

Advanced Laboratory Course
E215: Investigation of Particle-Antiparticle
Oscillations at Belle II

Amelia Carina de Lope Fend, Martin Ludwig

14.04.2025

Contents

1	Introduction	1
2	Experimental Setup	2
2.1	SuperKEKB	2
2.2	Belle II Detector	2
3	Reaction Identification via the Event Display	4
3.1	$e^+e^- \rightarrow \gamma\gamma$	4
3.2	$e^+e^- \rightarrow e^+e^-$	5
3.3	$e^+e^- \rightarrow \mu^+\mu^-$	5
3.4	$e^+e^- \rightarrow \tau^+\tau^-$	5
3.5	$e^+e^- \rightarrow \Upsilon(4S) \rightarrow B\bar{B}$	7
3.6	$e^+e^- \rightarrow q\bar{q}$	7
4	Particle Reconstruction	9
4.1	Decay Diagram and Properties of the Involved Particles	9
4.2	Data Set and Analysis Procedure	10
4.3	Reconstruction of the D^0	11
4.4	Reconstruction of the D^{*+}	15
4.5	Reconstruction of the \bar{B}^0	18
5	Determination of the $B^0\bar{B}^0$ Oscillation Frequency	23
5.1	Theoretical Considerations	23
5.2	Frequency Measurement	24
6	Conclusion	26
	List of Figures	27
	List of Tables	27
	Bibliography	28

1 Introduction

Our knowledge of the fundamental building blocks of matter comes from particle-physics experiments in which accelerated particles collide and produce multiple secondary particles. To reconstruct the reactions that occur during and shortly after the collision, the decay products must be identified via particle detectors and the intermediate states reconstructed in the data analysis.

In this experiment, this process will be demonstrated using simulated data from the Belle II experiment located at SuperKEKB in Japan. This accelerator collides electrons and positrons and operates at the $\Upsilon(4S)$ resonance, which decays into B mesons. Therefore, the facility is ideally suited for studying B physics. In particular, $B^0\bar{B}^0$ oscillations can be examined, which is the aim of this experiment. For this purpose, we consider the common decay chain $\bar{B}^0 \rightarrow D^{*+}l^-\bar{\nu}_l$, followed by $D^{*+} \rightarrow D^0\pi^+$ and $D^0 \rightarrow K^-\pi^+$, where we reconstruct the intermediate particles step by step and ultimately determine the number of oscillated B mesons.

This report is structured as follows: Chapter 2 provides information on the experimental setup, including the SuperKEKB accelerator and the Belle II detector. In Chapter 3, the Belle II event display is introduced and it is explained how different reaction types can be distinguished using it. The main part of the analysis is described in Chapter 4, where the B mesons are reconstructed step by step via their decay products. Finally, in Chapter 5, the number of oscillated B mesons is determined and plotted against the time difference between the B decays to extract the oscillation frequency. Chapter 6 summarizes the results.

2 Experimental Setup

The Belle II experiment is designed to perform precise measurements of the properties of B mesons and their decay products. It is located at the SuperKEKB accelerator, which is part of the High Energy Accelerator Research Organization (KEK) in Japan. In the following section, the basic design and working principles of both the accelerator and the detector are described. Unless stated otherwise, all presented information is taken from [1] and [2].

2.1 SuperKEKB

The SuperKEKB accelerator collides electrons and positrons at a center-of-mass energy of 10.58 GeV, corresponding to the mass of the $\Upsilon(4S)$ resonance [3]. The Υ mesons are bottomonium ($b\bar{b}$) states with quantum numbers $J^{PC} = 1^{--}$. While the lower Υ states lie below the open bottom threshold¹, the $\Upsilon(4S)$ state is heavy enough to decay into B mesons. In approximately half of the cases, it decays into B^+B^- and in the other half into $B^0\bar{B}^0$. Such an accelerator, which is optimized for the production of B mesons, is known as a B-factory.

SuperKEKB uses an asymmetric beam energy configuration, accelerating electrons to 7 GeV and positrons to 4 GeV. As a result, the $\Upsilon(4S)$ resonance is not produced at rest but is boosted along the z -axis (beam axis). Since the $\Upsilon \rightarrow B^0\bar{B}^0$ decay provides little available phase space, the resulting B mesons also travel almost along the z -direction. This characteristic is considered in the detector design and allows, for example, a precise determination of the time difference between the two B meson decays.

2.2 Belle II Detector

The Belle II detector comprises several subdetectors, each sensitive to a different class of particles (see Figure 2.1).

At its core is the **vertex detector (VXD)**, which directly surrounds the beam pipe. It delivers very high spatial resolution and is used to reconstruct the decay vertices of short-lived particles, such as B mesons.

This is followed by the **central drift chamber (CDC)**, which provides charged-particle tracking. The CDC is filled with a gas mixture that gets ionized when a charged particle passes through, allowing for the measurement of its trajectory. Since the entire

¹If a hadron has a non-zero net bottomness, like a B meson, it is referred to as an "open bottom" particle.

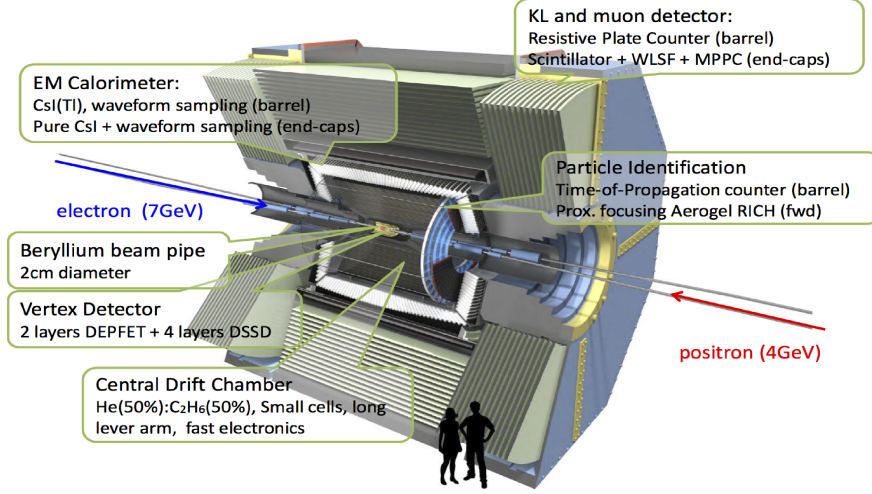


Figure 2.1: Overview of the Belle II detector. Figure taken from [4].

inner detector volume is immersed in a 1.5 T solenoidal magnetic field, these trajectories are curved, and the curvature can be used to determine each particle's momentum.

In addition to momentum, one must also measure a particle's velocity to determine its mass and hence its type. This **particle identification (PID)** is achieved with a time-of-propagation (TOP) counter and a ring-imaging Cherenkov (RICH) detector.

While the aforementioned detectors can detect and identify most charged particles, they are not sensitive to neutral particles such as photons or neutrons. These particles, however, are stopped in the **electromagnetic calorimeter (ECL)**. This detector consists of CsI(Tl) scintillator crystals, in which the particles initiate electromagnetic showers so that their energy deposition can be measured.

Finally, the outer layers and endcaps of the Belle II detector are dedicated to K_L^0 **and muon detection (KLM)**. Unlike other particles (except neutrinos, which cannot be measured directly), most long-lived kaons and muons are not stopped by the inner detector components. Therefore, the KLM consists of multiple layers of scintillators and resistive plate chambers (RPCs), which measure the energy deposition and velocity of these particles, respectively.

3 Reaction Identification via the Event Display

Although the SuperKEKB accelerator is tuned to the $\Upsilon(4S)$ resonance, other reactions can occur as well. These include the production of a quark–antiquark pair, a lepton–antilepton pair, or two photons from the e^+e^- collision. In this part of the experiment, we are provided with six files containing sets of simulated Belle II events, each corresponding to a specific process. Using the Belle II event display software, we aim to identify each process. This software depicts the interaction of particles with the detector: the trajectories of charged particles are marked in blue, interactions with the calorimeter are displayed as red lines, and hits in the KLM are represented by green rectangles.

3.1 $e^+e^- \rightarrow \gamma\gamma$

The easiest reaction to identify is the production of two photons. As they carry no electric charge, we expect them to leave no signature in the tracker. Instead, they deposit their energy in the calorimeter. Due to momentum conservation, the photons should be detected approximately in opposite directions (though not exactly, as they are not produced at rest). An example of such an event is shown in Figure 3.1.

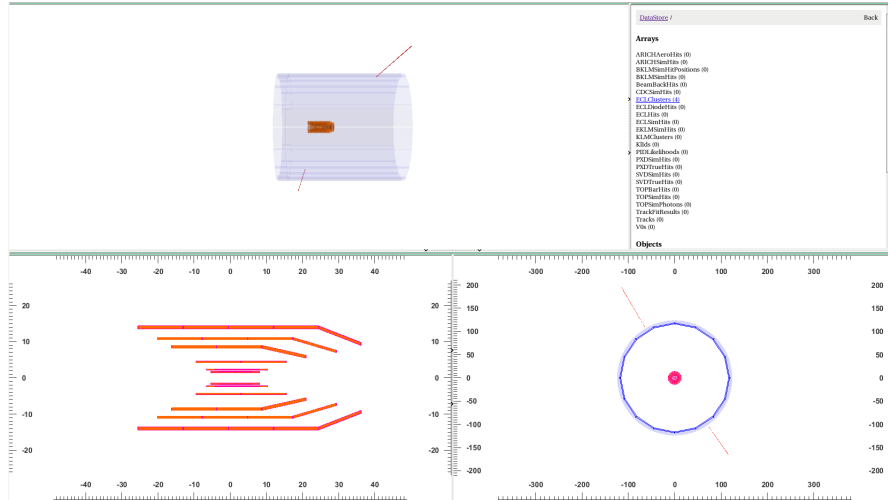


Figure 3.1: Event display for process identified as $e^+e^- \rightarrow \gamma\gamma$.

3.2 $e^+e^- \rightarrow e^+e^-$

Another process that is relatively simple to identify is e^+e^- production (Bhabha scattering). Due to their charge, we expect the electron and positron to leave curved tracks in the tracker with opposite curvature. Again, they should travel approximately in opposite directions according to momentum conservation. In the electromagnetic calorimeter, electrons and positrons initiate showers and are therefore stopped there. An example of this is shown in Figure 3.2.

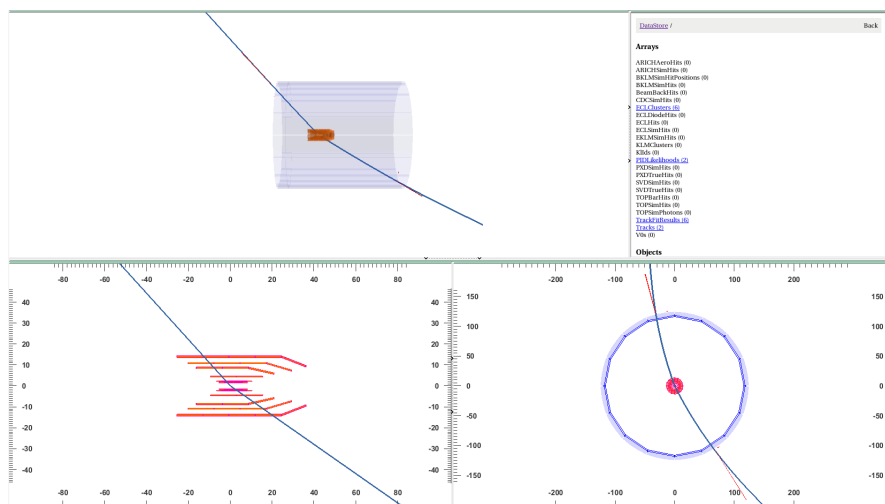


Figure 3.2: Event display for process identified as $e^+e^- \rightarrow e^+e^-$.

3.3 $e^+e^- \rightarrow \mu^+\mu^-$

Analogously to the electron-positron pair, we expect the muon-antimuon pair to leave charged tracks with opposite curvature in the tracker. However, we expect a different behavior when considering the calorimeter. As muons are significantly heavier than electrons, they lose less energy in matter. Thus, they are not stopped in the calorimeter but in the KLM. An example of this is shown in Figure 3.3.

3.4 $e^+e^- \rightarrow \tau^+\tau^-$

In contrast to the muons and electrons considered above, tau leptons are not sufficiently long-lived to leave tracks in the tracker. Instead, their decay products are detected. There is a large number of possible decay modes, but the most prevalent ones are the three-body decays $\tau^- \rightarrow e^- \bar{\nu}_e \nu_\tau$ and $\tau^- \rightarrow \mu^- \bar{\nu}_\mu \nu_\tau$ [3]. Among the final-state particles, only the electron or muon is detected.

If both taus decay into the same lepton, the event display is similar to those showing lepton-antilepton production in Sections 3.2 and 3.3. However, the angle between the

3.5 $e^+e^- \rightarrow \Upsilon(4S) \rightarrow B\bar{B}$

The processes $e^+e^- \rightarrow q\bar{q}$ and $e^+e^- \rightarrow \Upsilon(4S) \rightarrow B\bar{B}$ are not easy to distinguish, as both display a larger number of tracks than the lepton production considered above. However, for $e^+e^- \rightarrow \Upsilon(4S) \rightarrow B\bar{B}$ the mass of the $\Upsilon(4S)$ is very close to the center of mass energy, and the mass of the B-meson pair is only slightly below the mass of the $\Upsilon(4S)$. Therefore this process doesn't provide enough energy for jets to form. This corresponds to a higher radial symmetry in the x-y plane. Additionally, on average the decay chain of the B-mesons is longer than the decay chain of the hadrons produced in the quark anti-quark production. This translates to a higher number of tracks for the $e^+e^- \rightarrow \Upsilon(4S) \rightarrow B\bar{B}$ process. The number of tracks corresponds to the parameter listed as `TrackFitResults`. An example of this is shown in Figure 3.5.

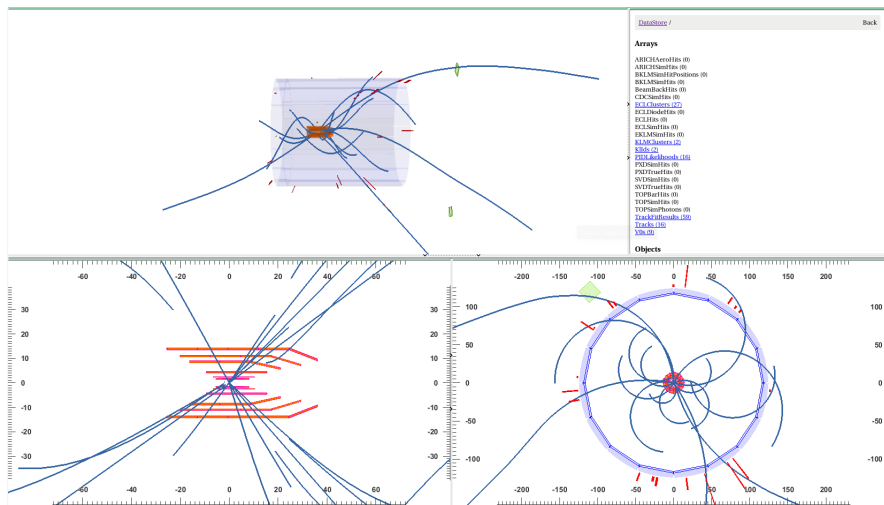
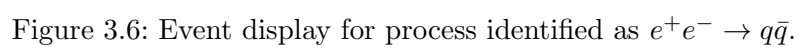


Figure 3.5: Event display for process identified as $e^+e^- \rightarrow \Upsilon(4S) \rightarrow B\bar{B}$.

3.6 $e^+e^- \rightarrow q\bar{q}$

A $q\bar{q}$ will hadronize after production and form jets. As discussed in Section 3.5, we expect a higher radial symmetry in the x-y plane but a smaller number of tracks for this process when compared to $e^+e^- \rightarrow \Upsilon(4S) \rightarrow B\bar{B}$. An example of this is shown in Figure 3.6.



4 Particle Reconstruction

4.1 Decay Diagram and Properties of the Involved Particles

As stated earlier, the aim of this experiment is to determine the $B^0\bar{B}^0$ oscillation frequency. To achieve this, the neutral B mesons must first be reconstructed via their decay products. For this purpose, we consider the decay chain depicted in Figure 4.1. Among the many possible B decays, this particular one has the advantage that the respective branching ratios are relatively large and the final state is well-detectable, as it contains only pions, kaons, and leptons (neglecting the undetectable neutrinos).

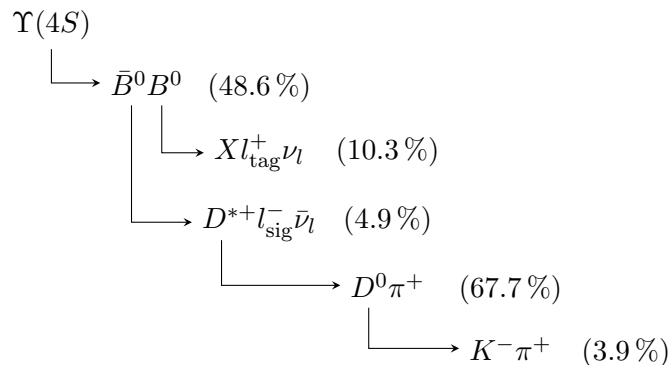


Figure 4.1: Decay diagram for the $\Upsilon(4S)$ state. The branching ratios given in parentheses are taken from [3].

To distinguish between the B meson that will be reconstructed via the given decay chain and the other B meson decaying via an unspecified semi-leptonic decay mode, the first is called the ‘signal’ and the latter the ‘tag’ B . The corresponding leptons are labeled in the same manner. Since it is not known a priori which lepton is which, the data set contains each event twice, with the signal and tag leptons interchanged.

While Figure 4.1 explicitly shows only the \bar{B}^0 decay chain, the B^0 can obviously decay in the same way, but with the corresponding antiparticles. For the sake of clarity, we will always refer to the \bar{B}^0 decay chain when naming particles in the following analysis. However, the respective antiparticles are also implicitly meant. In particular, all cuts for event selection are formulated in such a way that they apply equally to both the \bar{B}^0 and the B^0 decay chains.

In addition to the decay diagram, some knowledge about the resulting particles is necessary to reconstruct the intermediate states. Table 4.1 lists the masses and mean

lifetimes of the mesons appearing in the decay diagram in Figure 4.1. It can be seen that the charged pions and kaons are the lightest and longest-lived particles, which is why they are detected in the final state.

While the ground-state D and B mesons decay via the weak interaction and have lifetimes on the order of 10^{-12} seconds, the D^* decays via the strong interaction, resulting in a lifetime that is eight orders of magnitude shorter. Furthermore, it should be noted that the D^* is only slightly heavier than the combined mass of a D^0 and a pion ($m_{D^*} - m_{D^0} - m_\pi \approx 5 \text{ MeV}$), meaning that there is little phase space available for the D^* decay. As a result, the emerging pion is only relatively slow and can be well distinguished from the fast pion originating from the D^0 decay.

Table 4.1: Properties of the emerging mesons. Data taken from [3]. For the $D^{*\pm}$, the PDG reports the resonance width Γ . In this case, the mean lifetime was calculated via $\tau = \hbar/\Gamma$.

particle	mass	mean lifetime
π^\pm	140 MeV	$2.6 \times 10^{-8} \text{ s}$
K^\pm	494 MeV	$1.2 \times 10^{-8} \text{ s}$
D^0, \bar{D}^0	1865 MeV	$4.1 \times 10^{-13} \text{ s}$
D^\pm	1870 MeV	$1.0 \times 10^{-12} \text{ s}$
$D^{*\pm}$	2010 MeV	$7.9 \times 10^{-21} \text{ s}$
B^0, \bar{B}^0	5280 MeV	$1.5 \times 10^{-12} \text{ s}$

4.2 Data Set and Analysis Procedure

The provided data set consists of simulated data for five particle tracks: the signal and tag leptons, the kaon, and the two pions. For each track, the data frame contains information about its energy, momentum, charge, and the z -coordinate of its origin. In total, the set comprises 2.46 million events. For the analysis, the data file is read into a `pandas` DataFrame. All analysis steps are performed in a `Jupyter Notebook`, which can be found at <https://github.com/martludw/Advanced-Lab-Course/tree/main/E215>.

Invariant Mass

The most important concept for obtaining intermediate states from final-state particles is the **invariant mass**: Consider a particle with four-momentum vector $p = (E, \mathbf{p})$. Then, according to the relativistic energy-momentum relation, squaring p yields the invariant mass:

$$p^2 = p^\mu p_\mu = E^2 - \mathbf{p}^2 = m^2 \quad (\text{natural units: } c = 1)$$

Now consider a particle decay $A \rightarrow B + C$. Since four-momentum is conserved in all decays, we can reconstruct the four-momentum and consequently the mass of A via its

decay products:

$$p_A = p_B + p_C \quad m_A = \sqrt{(E_A + E_B)^2 - (\mathbf{p}_A + \mathbf{p}_B)^2} \quad (4.1)$$

In the following analysis, this technique will be used to reconstruct the D^0 , the D^* and the B^0 .

Signal Purity

When calculating the invariant masses of intermediate states, the results will be distributed around the true particle mass, as the energies and momenta measured by the detector are not perfectly accurate. As a consequence, a signal peak with a finite width appears in the invariant mass spectrum. Usually, this peak sits on top of some background caused by false particle combinations. To quantify how much the peak stands out from the background, one defines the **purity** α as the ratio between the number of actual signal events N_{sig} and the total number of candidate events N_{cand} (signal and background) in the signal region:

$$\alpha = \frac{N_{\text{sig}}}{N_{\text{cand}}} . \quad (4.2)$$

In general, the goal of a particle physics analysis is to reconstruct intermediate states with high purity. For this, one has to find reasonable constraints that remove background without discarding too many signal events. What purities are regarded as good depends on the specific task. According to [1], with the given data set, a purity above 65 % for the D^0 reconstruction and a purity above 80 % for the D^{*+} reconstruction should be achievable.

4.3 Reconstruction of the D^0

As a first analysis step, we calculate for each event the invariant mass of the D^0 from the four-momentum vectors of the π^+ and the K^- . After plotting the result as a histogram, a clear peak around the true D^0 mass is visible, standing out from some background. This background can be reduced by applying reasonable restrictions on the properties of the kaons and pions. One obvious choice for such a restriction is the requirement that the kaon and pion must have opposite charges. Furthermore, they should originate from the same z -coordinate, namely the D^0 decay point. As there is, of course, some variation due to the detector's spatial resolution, we plotted the position difference Δz as a histogram and concluded that 0.125 cm is a good choice for an upper boundary on Δz . By applying these two constraints, the background could be reduced significantly, as shown in Figure 4.2.

In order to determine the purity of the peak after applying the constraints, we first have to identify the signal range. To do this, we fit a Cauchy (Lorentz) distribution

$$f(x) = A \cdot \frac{\gamma}{(x - x_0)^2 + \gamma^2} \quad (4.3)$$

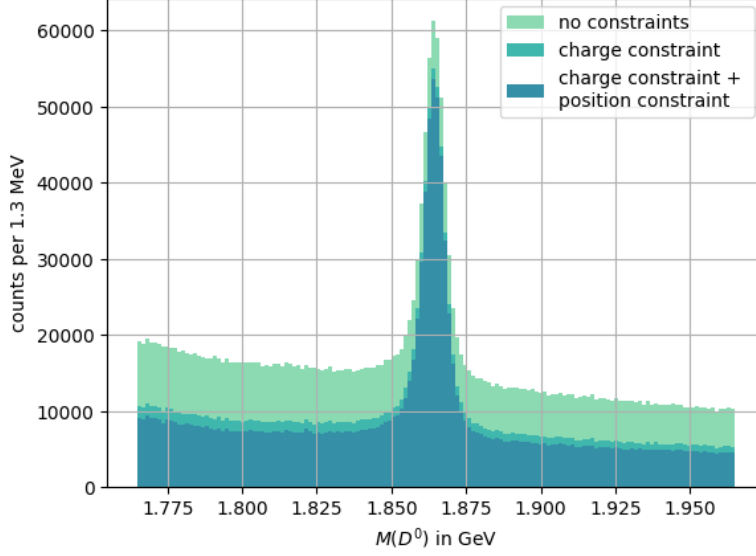


Figure 4.2: Invariant mass of the D^0 , obtained from the π^+ and the K^- according to Eq. 4.1.

to the peak, where x_0 is the peak position, γ denotes the half width at half maximum (HWHM), and A is an overall scaling related to the amplitude ($f(x_0) = A/\gamma$). The fit result is shown in Figure 4.3a.

We then define a 3γ interval around the determined peak position as the signal region. To estimate the number of background events in this region, we exclude a 6γ interval around the peak position from the histogram and fit the remaining events with a linear function:

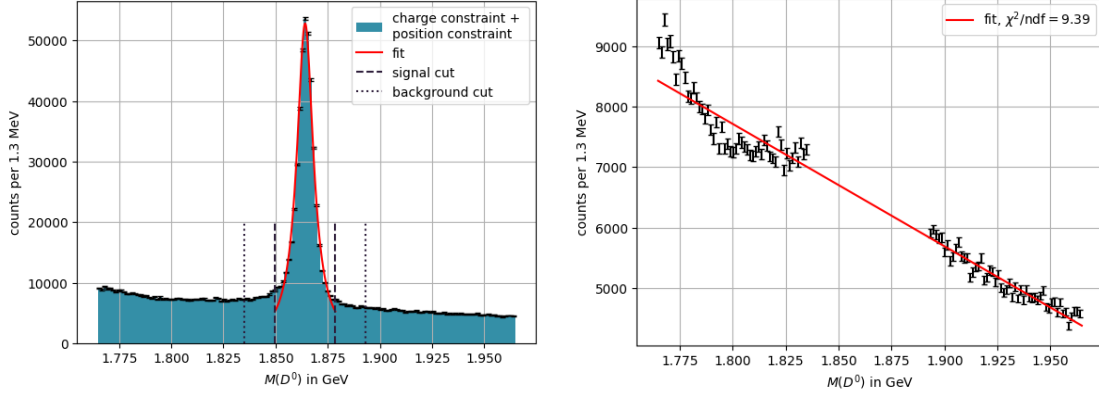
$$g(x) = a \cdot x + b, . \quad (4.4)$$

The result is displayed in Figure 4.3b. While the fit describes the background on the right-hand side of the peak very well, the background on the left-hand side appears to exhibit a more complex behavior, which explains the relatively poor fit quality of $\chi^2/\text{ndf} = 9.39$. However, we chose not to use a more complex background model to avoid overfitting. Moreover, the fitted function still seems to provide a reasonable estimate for the number of background events in the signal region, and we do not expect a more sophisticated fit to significantly affect this number or the resulting purity.

Having determined the signal region and the number of background events, we can compute the peak's purity according to Eq. 4.2. Specifically, N_{cand} is the total number of events in the signal region, and N_{sig} is this number minus the estimated number of background events. This yields

$$\alpha = 72(4) \%,$$

where the uncertainty was calculated using Gaussian error propagation, assuming a statistical uncertainty of \sqrt{N} for the histogram bin entries and taking into account the



(a) Invariant mass of the D^0 fitted with a Cauchy distribution (Eq. 4.3). The obtained fit-parameters are: $A = 255(6)$, $x_0 = 1864.18(13)$ MeV, $\gamma = 4.82(18)$ MeV. (b) Background events fitted with a linear function (Eq. 4.4). The obtained fit-parameters are: $a = -2.029(35) \times 10^4 \text{ GeV}^{-1}$, $b = 4.42(7) \times 10^4$.

Figure 4.3: Purity determination of the D^0 invariant mass peak. The signal region was determined by a 3γ interval around the peak position (‘signal cut’), while for the background fit, a 6γ interval around peak was excluded (‘background cut’).

uncertainties of the background fit parameters. According to [1], a purity greater than 65 % is considered good for the D^0 invariant mass, indicating that our event selection is effective.

For all further analysis steps, we only consider events that satisfy the charge and position constraint from Figure 4.2 and additionally lie in the determined signal region.

Momentum Consideration

To verify that the invariant mass peak actually contains the searched-for events, we can calculate the average momentum of the reconstructed D^0 and compare it with theoretically expected values. To calculate an expectation value of a quantity x on a data sample that contains both signal and background events, we apply the formula given in [1]:

$$\langle x \rangle_{\text{cand}} = \alpha \cdot \langle x \rangle_{\text{sig}} + (1 - \alpha) \cdot \langle x \rangle_{\text{bgd}},$$

where α is the purity and the subscripts indicate that the average value is calculated over all candidates, over signal events, or over background events only. In our case, the quantity of interest is $|\mathbf{p}_{D^0}|$ and our aim is to determine $\langle |\mathbf{p}_{D^0}| \rangle_{\text{sig}}$. Thus, we find:

$$\langle |\mathbf{p}_{D^0}| \rangle_{\text{sig}} = \frac{\langle |\mathbf{p}_{D^0}| \rangle_{\text{cand}} - (1 - \alpha) \cdot \langle |\mathbf{p}_{D^0}| \rangle_{\text{bgd}}}{\alpha}. \quad (4.5)$$

Practically, we use the peak region to calculate $\langle |\mathbf{p}_{D^0}| \rangle_{\text{cand}}$ and the sidebands to calculate $\langle |\mathbf{p}_{D^0}| \rangle_{\text{bgd}}$. As an estimator for the uncertainties of the averages we use the sample

standard deviation divided by the square root of the sample's size. Inserting these values and the previously determined purity into Eq. 4.5, we obtain

$$\langle |\mathbf{p}_{D^0}| \rangle_{\text{sig}} = 1.701(19) \text{ GeV}.$$

Now, we want to compare this result to theoretical predictions. For this, we consider two cases: A D^0 originating from the decay chain $\bar{B}^0 \rightarrow D^{*+} \ell^- \bar{\nu}, D^{*+} \rightarrow D^0 \pi^+$ and another D^0 originating from a hadronic B decay $\bar{B}^0 \rightarrow D^0 \pi^0$. Since the latter is a two-body decay, it can be solved exactly: Let $p_{\bar{B}^0}$, p_{D^0} and p_{π^0} be the four-momenta of the three particles, respectively. Four-momentum conservation implies $p_{\bar{B}^0} = p_{D^0} + p_{\pi^0}$. If we are in the \bar{B}^0 rest frame, then $p_{\bar{B}^0} = (m_{B^0}, 0)$ and thus

$$\begin{aligned} m_{\pi^0}^2 &= p_{\pi^0}^2 = (p_{\bar{B}^0} - p_{D^0})^2 \\ &= p_{\bar{B}^0}^2 + p_{D^0}^2 - 2p_{\bar{B}^0} p_{D^0} \\ &= m_{B^0}^2 + m_{D^0}^2 - 2m_{B^0} E_{D^0} \\ \iff E_{D^0} &= \frac{m_{B^0}^2 + m_{D^0}^2 - m_{\pi^0}^2}{2m_{B^0}}. \end{aligned}$$

Using $\mathbf{p}_{D^0}^2 = E_{D^0}^2 - m_{D^0}^2$ and relabeling the D^0 momentum as $\mathbf{p}_{D^0}^{\text{hadr}}$ to distinguish the hadronic and semi-leptonic mode, we arrive at

$$|\mathbf{p}_{D^0}^{\text{hadr}}| = \frac{\sqrt{(m_{B^0}^2 + m_{D^0}^2 - m_{\pi^0}^2)^2 - 4m_{B^0}^2 m_{D^0}^2}}{2m_{B^0}}. \quad (4.6)$$

Inserting $m_{B^0} = 5279.72 \text{ MeV}$, $m_{D^0} = 1864.84 \text{ MeV}$ and $m_{\pi^0} = 134.98 \text{ MeV}$ taken from [3] gives $|\mathbf{p}_{D^0}^{\text{hadr}}| = 2308.30 \text{ MeV}$ in the \bar{B}^0 rest frame. Using a boost of $\beta = 0.28$ in z-direction, we can use a Lorentz transformation to compute an upper and lower bound on the D^0 momentum in the lab frame. This is done by assuming that the D^0 momentum in the rest frame is directed parallel or anti-parallel to the z-axis, and thus $p_{z,D^0}^{\text{hadr}} = \pm |\mathbf{p}_{D^0}^{\text{hadr}}|$

$$p_{z,D^0,\text{lab}}^{\text{hadr}} \in \left[\gamma \left(\beta E_{D^0} + |\mathbf{p}_{D^0}^{\text{hadr}}| \right), \gamma \left(\beta E_{D^0} - |\mathbf{p}_{D^0}^{\text{hadr}}| \right) \right], \quad (4.7)$$

where γ is the Lorentz factor $\gamma = \frac{1}{\sqrt{1-\beta^2}}$. This yields

$$p_{z,D^0,\text{lab}}^{\text{hadr}} \in [-1536.48 \text{ MeV}, 3269.77 \text{ MeV}].$$

for the z-component, while the x and y component remain unchanged after boosting. Thus the maximal and minimal absolute momenta are achieved if in the momentum in the rest frame directed parallel or anti-parallel to the z-axis and lie in the interval of

$$|\mathbf{p}_{D^0,\text{lab}}^{\text{hadr}}| \in [1536.48 \text{ MeV}, 3269.77 \text{ MeV}].$$

The semi-leptonic decay $\bar{B}^0 \rightarrow D^{*+} (\rightarrow D^0 \pi^+) \ell^- \bar{\nu}$ is more complicated, as it is a three body decay. It also involves an anti-neutrino, which is not detected at Belle II.

Therefore the exact value for the momentum of the D^0 can not be predicted theoretically, but we can still estimate an upper limit. Assuming the anti-neutrino is produced at rest $\vec{p}_\nu = \vec{0}$, we can derive an upper limit on the momentum of the D^0 . For this we will also use $m_\nu \approx 0$. In this case, the two body decay formula derived above (Equation 4.6) applies. We will first use it to reconstruct the D^{*+} momentum and then use this result to derive the D^0 . Thus using $m_{D^{*+}} = 2010.26 \text{ MeV}$ [3] yields

$$|\mathbf{p}_{D^{*+}}| \leq \frac{\sqrt{(m_{B^0}^2 + m_{D^*}^2 - m_\ell^2)^2 - 4m_{B^0}^2 m_{D^*}^2}}{2m_{B^0}}.$$

Here out of $\ell^- \in \{e^-, \mu^-, \tau^-\}$ the electron mode gives the upper bound and inserting its mass gives $|\mathbf{p}_{D^{*+}}| \leq 2257.02 \text{ MeV}$ in the rest frame of the B^0 . The upper limit on the momentum in the lab frame is achieved if the D^{*+} momentum and the resulting D^0 are parallel to the z-axis. After applying the lorentz boost (Equation 4.7) for this scenario, this results in an upper bound for the lab frame momentum of $|\mathbf{p}_{D^{*+}}^{\text{lab}}| \leq 3232.54 \text{ MeV}$. This corresponds to a maximal boost in z-direction of β' (from D^{*+} rest frame to lab frame) of

$$\beta' = \frac{|\mathbf{p}_{D^{*+}}^{\text{lab}}|}{E_{D^{*+}}^{\text{lab}}} = 0.85.$$

In the rest frame of the D^{*+} , using Equation 4.6, we can derive the D^0 moment of the semi-leptonic mode. For $m_{\pi^+} = 139.57 \text{ MeV}$ [3] this yields

$$|\mathbf{p}_{D^0, D^{*+} \text{rf}}^{\text{semi-lep}}| \leq \frac{\sqrt{(m_{D^*}^2 + m_{D^0}^2 - m_{\pi^+}^2)^2 - 4m_{D^*}^2 m_{D^0}^2}}{2m_{D^*}} = 39.89 \text{ MeV}.$$

Finally, we can apply the boost β' and obtain an upper bound of

$$|\mathbf{p}_{D^0, \text{lab}}^{\text{semi-lep}}| \leq 3084 \text{ MeV}.$$

The average momentum $\langle |\mathbf{p}_{D^0}| \rangle_{\text{sig}} = 1.7 \text{ GeV}$ calculated above appears to be consistent with these estimations. It lies within the interval of possible absolute momenta found for the two body decay and below the upper limit found for the three body decay.

4.4 Reconstruction of the D^{*+}

Before calculating the D^{*+} invariant mass, we want to study the decay $D^{*+} \rightarrow D^0 \pi^+$ in a little more detail. As explained in Section 4.1, there is only very little phase space for the D^{*+} decay, which affects the momenta of its decay products. In the D^{*+} rest frame, the decay particles fly, of course, back-to-back with the same absolute momentum. Since this decay momentum is generally much smaller than the momentum of the D^{*+} , the decay products fly almost in the same direction in the lab frame. We can visualize this by plotting the D^0 momentum against the π^+ momentum in a histogram (see Figure 4.4). In the edge case of no transverse momentum between the D^0 and the π^+ , this

should yield a straight line whose slope is given by the ratio of the particles' masses: $m_{D^0}/m_{\pi^+} \approx 13$. In reality, due to the small but finite transverse momentum, this line is spread out into a narrow band. This exactly reflects the behavior observed in Figure 4.4.

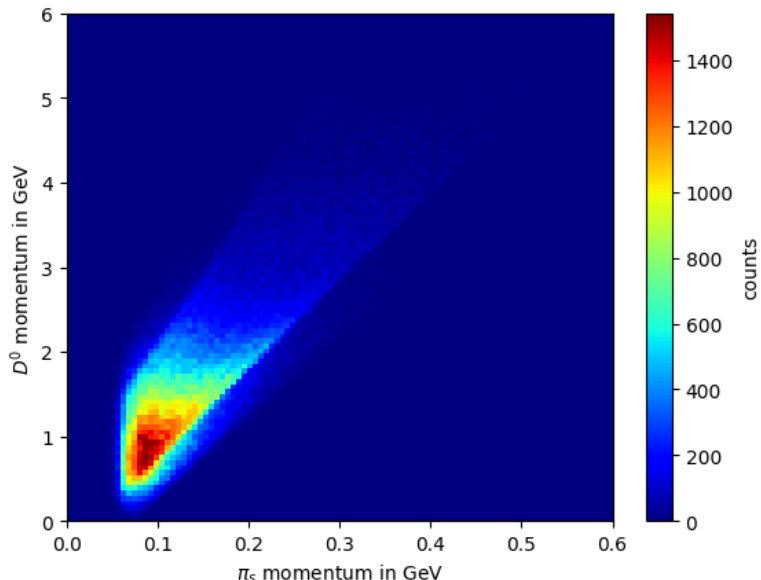


Figure 4.4: Correlation between the momenta of the D^0 and the slow pion π_s . The small phase space of the D^{*+} fixes the relative momenta of the decay products sharply.

After confirming our expectations regarding the D^0 and π^+ momenta, we can calculate and plot their invariant mass. The result is shown in Figure 4.5. It can be seen that the peak is centered around the true D^* mass but is relatively broad, spanning several tens of MeV. This is a consequence of combining two particles whose four-momenta both contain measurement uncertainties, particularly since the D^0 itself is already reconstructed from two other particles. The resulting mass resolution is thus a convolution of the uncertainties of all involved particles. Since it is almost impossible to find a reasonable distinction between signal and background in Figure 4.5, we need to come up with another approach.

Because a major reason for the poor mass resolution is the uncertainty on the D^0 four-momentum, we can instead plot the mass difference $M(D^{*+}) - M(D^0)$ (see Figure 4.6). In this way, the D^0 -related measurement errors largely cancel out (especially systematic errors such as detector calibration and alignment). As a result, the peak in the mass difference histogram shown in Figure 4.6 becomes much narrower, being dominated mainly by the slow pion measurement error.

As before, our aim in the analysis is to reduce the data sample by removing uninteresting background events. Before cutting away the sidebands in Figure 4.6, we can

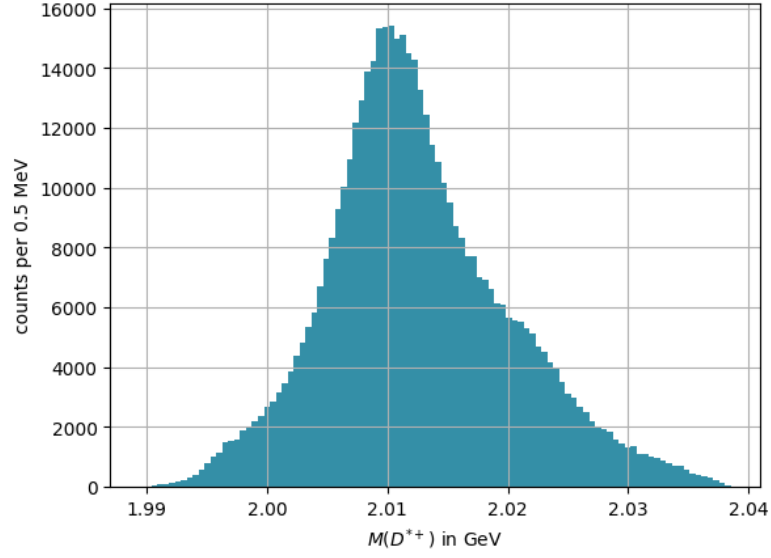


Figure 4.5: Invariant mass of the D^{*+} , obtained from the D^0 and the slow pion according to Eq. 4.1. The resulting peak is relatively broad.

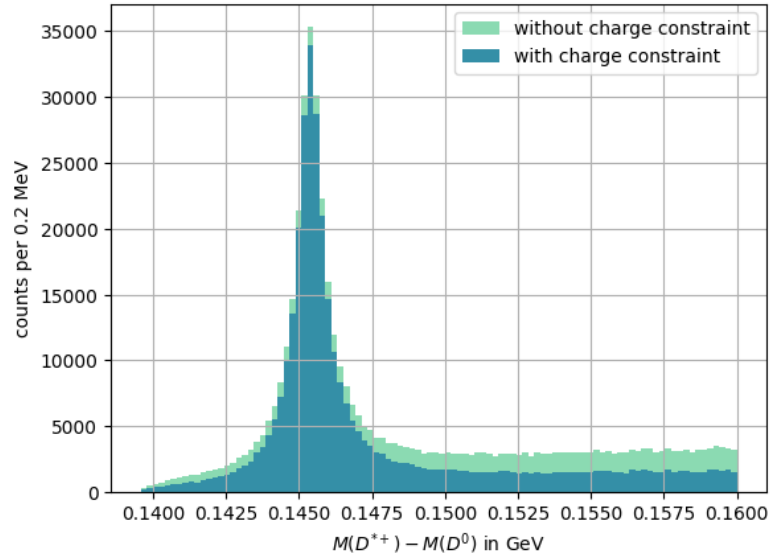


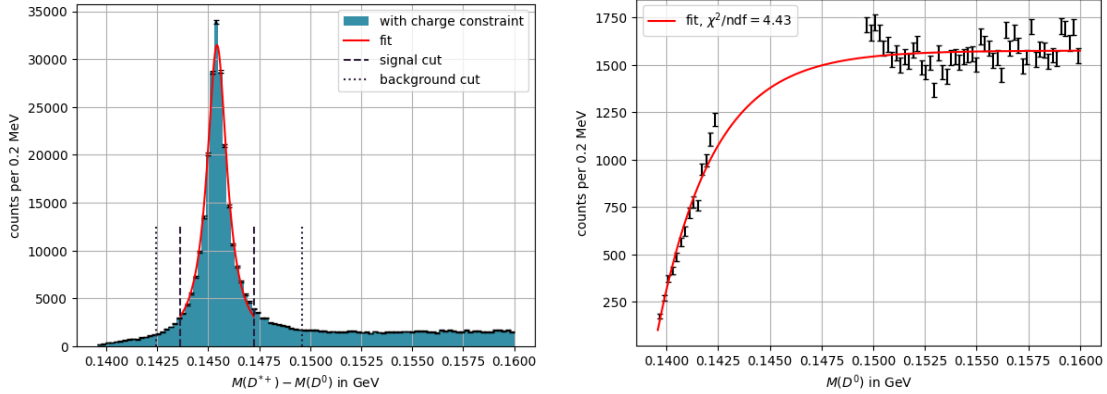
Figure 4.6: Difference of the invariant masses of the D^{*+} and the D^0 . As D^0 -related measurement errors cancel out, the resulting peak is much narrower.

further enhance the peak's purity by requiring that the charge of the slow pion be the same as the charge of the pion used for the D^0 reconstruction. This is shown by the blue histogram (labeled 'with charge constraint') in Figure 4.6.

For the purity determination, we proceed similarly to Section 4.3: First, we identify the signal region by fitting a Cauchy distribution to the peak, as depicted in Figure 4.7a. As before, a 3γ interval around the determined peak position is defined as the signal region. The background is then fitted with an exponentially flattening function

$$h(x) = a \cdot (1 - \exp(-b \cdot (x - c))) . \quad (4.8)$$

For the background fit, we exclude an asymmetric interval $[x_0 - 5\gamma, x_0 + 7\gamma]$ around the peak. The result is shown in Figure 4.7b. It can be seen that the fitted function describes the overall background behavior well.



(a) Difference of the invariant masses of the D^{*+} and the D^0 fitted with a Cauchy distribution (Eq. 4.3). The obtained fit-parameters are: $A = 255(6)$, $x_0 = 145.429(16)$ MeV, $\gamma = 0.599(20)$ MeV. (b) Background events fitted with a exponentially flattening function (Eq. 4.8). The obtained fit-parameters are: $a = 1574(12)$, $b = 0.370(20)$ MeV $^{-1}$, $c = 139.40(5)$ MeV.

Figure 4.7: Purity determination of the $M(D^{*+}) - M(D^0)$ mass difference peak. The signal region was determined by a 3γ interval around the peak position ('signal cut'). For the background fit, an asymmetric interval $[x_0 - 5\gamma, x_0 + 7\gamma]$ was excluded ('background cut').

With the total number of events in the signal region and the estimated number of background events, we can determine the purity according to Eq. 4.2. This yields

$$\alpha = 89.57(20) \% ,$$

where the uncertainty is calculated as before by propagating the fit parameter errors and assuming \sqrt{N} uncertainties for the bin entries. This exceeds the benchmark of 80 % given in [1], indicating that our event selection is effective.

4.5 Reconstruction of the \bar{B}^0

Having successfully reconstructed the D^{*+} and reduced the data set accordingly, we can now turn our attention to the B mesons. As explained in Section 4.1, we distinguish

between the signal and tag B mesons as well as between the corresponding leptons. The z_0 coordinates of the two leptons approximately correspond to the points at which the B mesons decayed. To get a sense of how close the B decays occur, we can plot the position difference $\Delta z_0 = z_0(\ell_s) - z_0(\ell_t)$ of the two leptons. The result is shown in Figure 4.8. Since the data set contains each event twice, with the signal and tag lepton interchanged, the distribution is exactly symmetric around zero. It can be seen that in the majority of plotted events, $|\Delta z_0|$ is smaller than 0.5 mm. This is consistent with the approximate distances we expect the B^0 mesons to fly ($c\tau = 455 \mu\text{m}$ [3]).

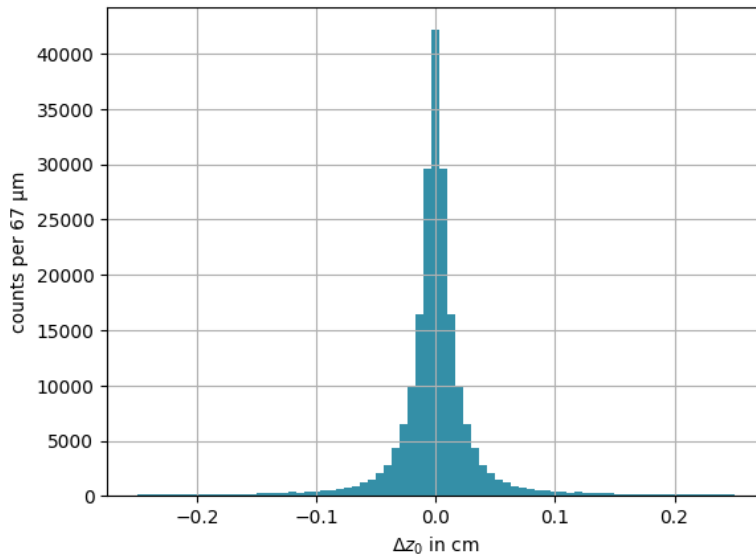


Figure 4.8: z_0 position difference between the signal and tag lepton's origin.

Next, we also consider the D^{*+} position. Since the D^{*+} decays almost instantaneously and the resulting D^0 also travels only a relatively short distance ($c\tau = 123 \mu\text{m}$ [3]) before it decays further, we approximate $z_0(D^{*+})$ by averaging over the z_0 coordinates of the kaon and the two pions. The resulting D^{*+} positions are visualized in Figure 4.9. Just like the z_0 coordinate of the signal lepton, $z_0(D^{*+})$ should indicate the position at which the signal B decayed. Thus, it makes sense that the histogram is slightly shifted towards positive z_0 values, since the B mesons typically travel a small distance in the z -direction before decaying.

As mentioned, the z_0 coordinate of the signal lepton ℓ_s and that of the D^{*+} should be approximately equal. Thus, if we plot $z_0(\ell_s)$ against $z_0(D^{*+})$ in a two-dimensional histogram, we expect a straight line through the origin. However, since we do not yet distinguish the signal lepton from the tag lepton and there are uncertainties in the determination of the z_0 positions (particularly, the estimation of $z_0(D^{*+})$ by averaging over the positions of its decay products is not exact), we expect this line to be smeared out, rather forming a blob. This behavior is visible in Figure 4.10.

With the help of these considerations, we can formulate several constraints for the

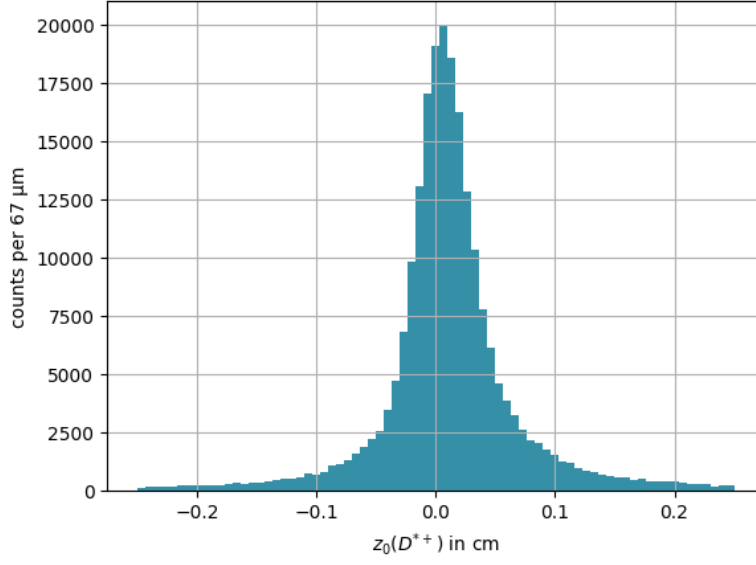


Figure 4.9: z_0 position of the D^{*+} .

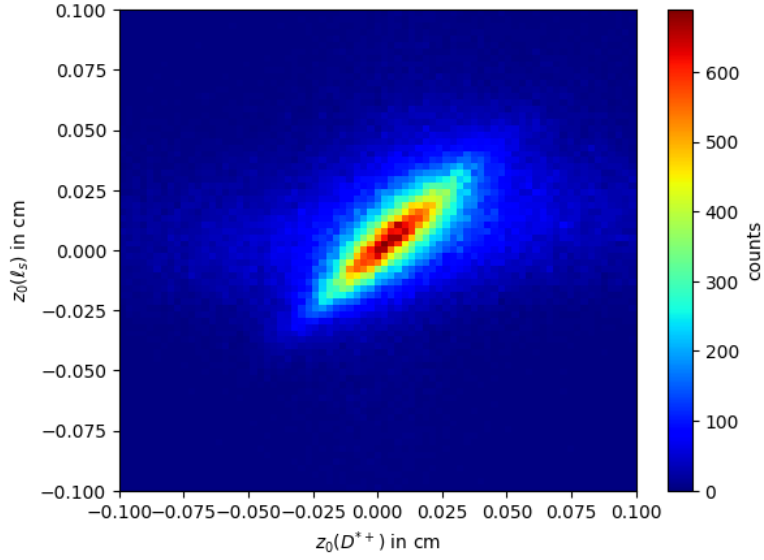


Figure 4.10: Correlation between the origins of the signal lepton ℓ_s and the D^{*+} .

final selection of neutral B meson candidates. First, we require that the total number of measured leptons per event equals two. This removes background from events in which the signal or tag lepton was not detected, or where the X in the B_{tag} decay chain (see Figure 4.1) also decays leptonically, making it even harder to correctly attribute the signal and tag leptons.

Next, we require that the absolute distance between the origins of the signal lepton and the D^{*+} be smaller than that between the tag lepton and the D^{*+} : $|z_0(\ell_s) - z_0(D^{*+})| < |z_0(\ell_t) - z_0(D^{*+})|$. Since each event appears twice in the dataset with the signal and tag leptons interchanged, this constraint halves the dataset and largely selects the events with correct signal/tag attribution.

Finally, we impose a condition on the lepton charges: if the signal and tag leptons have the same charge (in which case the B meson pair is considered oscillated, see Section 5.2), then the charge of the lepton must match the charge of the pions.

The effects of these cuts can be visualized by plotting the visible part of the \bar{B}^0 invariant mass. This means that we calculate and plot the invariant mass of the signal lepton and the D^{*+} , without considering the undetectable neutrino. The result is shown in Figure 4.11. The distribution is relatively broad, peaking between 2 and 3 GeV, and extending up to the actual B^0 mass. Some values even exceed the B^0 mass, which is unphysical and arises from measurement uncertainties in the particles' four-momenta. These unphysical entries are excluded from the determination of the oscillation frequency as well.

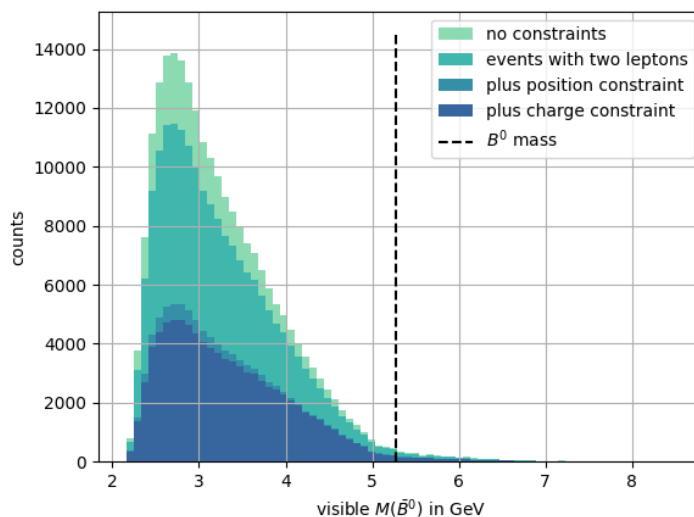


Figure 4.11: Visible part of the mass of the signal B^0 meson. It becomes visible how the different constraints reduce the data.

Finally, after applying all the selection criteria, we can replot Figure 4.10 to examine the impact of our constraints on the correlation between the origins of the signal lepton and the D^{*+} . The updated plot is shown in Figure 4.12. As expected, the correlation is now significantly more pronounced.

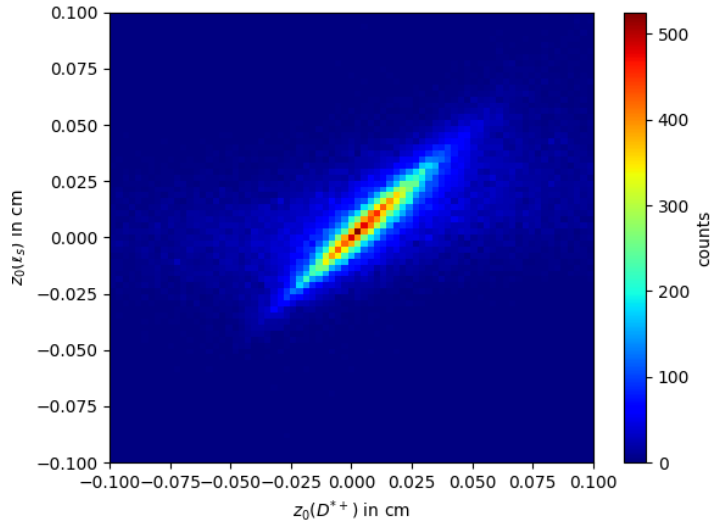


Figure 4.12: Correlation between the origins of the signal lepton ℓ_s and the D^{*+} after applying all selection criteria.

5 Determination of the $B^0\bar{B}^0$ Oscillation Frequency

Having reconstructed the full B meson decay chain, we are now capable to determine the $B^0\bar{B}^0$ oscillation frequency. Before doing so, Section 5.1 provides a brief introduction to the theory behind $B^0\bar{B}^0$ oscillations, clarifying the expected outcome of the measurement. Unless stated otherwise, all information presented in this theory section is taken from [1].

5.1 Theoretical Considerations

Since the eigenstates of the weak interaction are not identical to the mass eigenstates, the B^0 can oscillate into its antiparticle and vice versa. The leading-order contribution to this process is a second-order weak transition and involves two box diagrams, as shown in Figure 5.1.

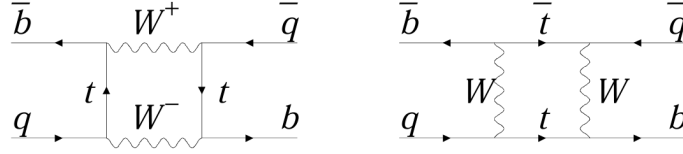


Figure 5.1: Box diagrams of leading order $B^0\bar{B}^0$ transitions. Taken from [5].

To describe the time evolution of the entangled $B^0\bar{B}^0$ pair produced in the $\Upsilon(4S)$ decay, we first consider the CP eigenstates $B_1 = \frac{1}{\sqrt{2}}(B^0 + \bar{B}^0)$ and $B_2 = \frac{1}{\sqrt{2}}(B^0 - \bar{B}^0)$. These states are expected to differ in mass by ΔM , however the difference in lifetime is negligible and will be assumed to be zero throughout this report. Assuming a decay rate Γ and a state B^0 at time $t = 0$, this results in a probability W_{B^0} of finding a B^0 after a time t of

$$W_{B^0}(t) = \frac{1}{2}e^{-\Gamma t}(1 + \cos(\Delta Mt))$$

and probability $W_{\bar{B}^0}$ of finding a \bar{B}^0 of

$$W_{\bar{B}^0}(t) = \frac{1}{2}e^{-\Gamma t}(1 - \cos(\Delta Mt)).$$

After a certain amount of time, a number of B -mesons N_{osc} will have oscillated into their anti-particles, while a number $N_{\text{non-osc}}$ remains in its initial state. To quantify the

mixing, we define the Asymmetry function \mathcal{A} and insert the oscillation probabilities to find

$$\mathcal{A}(t) = \frac{N_{\text{osc}}(t) - N_{\text{non-osc}}(t)}{N_{\text{osc}}(t) + N_{\text{non-osc}}(t)} = \cos(\Delta Mt). \quad (5.1)$$

In practice, we need to account for misidentified states, which can be caused by mistaging. Assuming a time independent misidentification probability of P_{wrong} , this would lead to measured number of oscillated states $N_{\text{osc, meas}}$ of

$$N_{\text{osc, meas}} = (1 - P_{\text{wrong}}) N_{\text{osc}} + P_{\text{wrong}} N_{\text{non-osc}}. \quad (5.2)$$

Inserting this into Eq. 5.1 provides how the measured asymmetry function differs from the true asymmetry function

$$\mathcal{A}_{\text{meas}}(t) = (1 - 2P_{\text{wrong}}) \cos(\Delta Mt), \quad (5.3)$$

where the factor $(1 - 2P_{\text{wrong}})$ is referred to as the dilution \mathcal{D} .

5.2 Frequency Measurement

In Chapter 4, we reconstructed the neutral B mesons. Within the final data set, we still need to distinguish the oscillated B mesons from the non-oscillated ones. To do this, we refer to the charge of the leptons in the semi-leptonic neutral B decays. If the leptons have opposite charges, we infer that the B meson pair did not oscillate. If the charges are the same, the pair has oscillated. Based on this criterion, we divide our data set into an oscillated and a non-oscillated subset.

To evaluate the asymmetry function, we require the time difference Δt between the decays of the two B mesons. This information is provided in the simulated data set and can be derived from the difference in z_0 -positions of the decays, which corresponds to the spatial separation of the leptons produced in the semi-leptonic B decays. Due to the exponential nature of the decay, the number of events with large Δt is significantly smaller than those with small Δt . As a result, the statistical uncertainties increase for large Δt , leading to large error bars. To mitigate this, we restrict our analysis to decays with $|\Delta t| \leq 10$ ps.

After applying this final constraint, we divide the oscillated and non-oscillated data sets into 50 time bins and compute the asymmetry function for each bin. To obtain the uncertainty, we assume a statistical uncertainty of \sqrt{N} on the bin entries and propagate this using Gaussian error propagation. According to the theoretical considerations of the previous Section 5.1, we fit a function

$$\mathcal{A}_{\text{meas}} = a \cdot \cos(\Delta M \Delta t) + b$$

to the data. The fit result is depicted in Figure 5.2 and we obtain the parameters

$$\begin{aligned} \Delta M &= 0.547(15) \text{ ps}^{-1} \\ a &= 0.155(7) \\ b &= 0.205(6). \end{aligned}$$

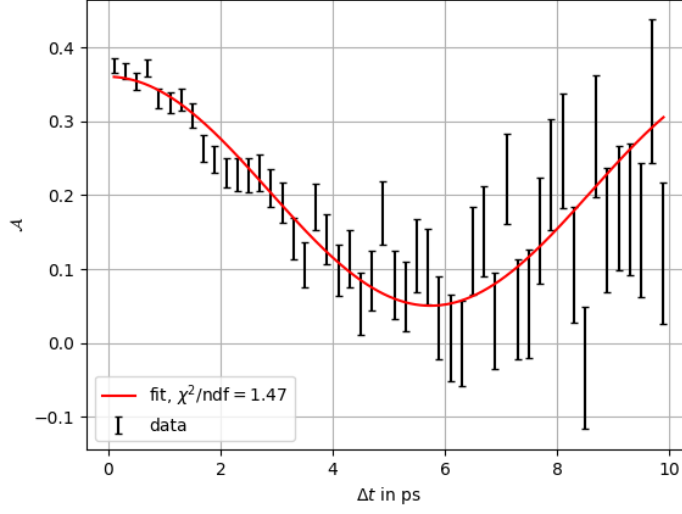


Figure 5.2: Asymmetry \mathcal{A} as a function of the time Δt between the two B decays. A least-square fit (red line) was performed to determine the oscillation frequency. The reduced χ^2 value being close to 1 implies a good fit quality.

The parameter a corresponds to the dilution $\mathcal{D} = (1 - 2P_{\text{wrong}})$. Thus, the misidentification probability is

$$P_{\text{wrong}} = 42.3(4) \, \%.$$

This is lower than the value obtained by randomly guessing, which corresponds to a misidentification probability of 50 %.

The offset b is not motivated by the theoretical considerations outlined in Section 5.1. A possible explanation could be the misidentification of charged B mesons as neutral ones. Since charged B mesons do not oscillate—because electric charge is conserved—they would only contribute to $N_{\text{non-osc}}$, leading to a positive offset that may increase slightly with time. Although our previous selection criteria should have significantly reduced the number of such misidentifications, they may not have eliminated them entirely.

We obtained a mass difference of $\Delta M = 0.547(15) \, \text{ps}^{-1}$. The value listed by the PDG is $\Delta M_{\text{lit}} = 0.5069(19) \, \text{ps}^{-1}$ [5], which lies within a 3σ interval of our result. The precision of our measurement could be improved with a larger data sample and more sophisticated selection criteria.

6 Conclusion

In this experiment, we analyzed simulated data from the Belle II experiment. In the first part, we used the Belle II event display to identify different types of particle reactions, including photon production, lepton–antilepton production, quark–antiquark production, and the $\Upsilon(4S)$ resonance.

The aim of the second part of the experiment was to determine the $B^0\bar{B}^0$ oscillation frequency. For this purpose, the B mesons had to be reconstructed step by step via their decay products. In our analysis, we considered the decay chain $\bar{B}^0 \rightarrow D^{*+}\ell^-\bar{\nu}$, $D^{*+} \rightarrow D^0\pi^+$ as it has a relatively large branching ratio and the final state is well-detectable. After the particle reconstruction, we identified oscillated and non-oscillated events based on the charges of the tag and signal leptons. From this, we obtained the asymmetry function as a function of time. To determine the oscillation frequency, a sinusoidal function was fitted to the asymmetry values. From this fit, we determined a mistagging probability of

$$P_{\text{wrong}} = 42.3(4) \%$$

as well as a mass difference between the CP eigenstates of

$$\Delta M = 0.547(15) \text{ ps}^{-1},$$

which deviates by approximately three σ from the value listed by the PDG.

List of Figures

2.1	Overview of the Belle II detector.	3
3.1	Event display for process identified as $e^+e^- \rightarrow \gamma\gamma$	4
3.2	Event display for process identified as $e^+e^- \rightarrow e^+e^-$	5
3.3	Event display for process identified as $e^+e^- \rightarrow \mu^+\mu^-$	6
3.4	Event display for process identified as $e^+e^- \rightarrow \tau^+\tau^-$	6
3.5	Event display for process identified as $e^+e^- \rightarrow \Upsilon(4S) \rightarrow B\bar{B}$	7
3.6	Event display for process identified as $e^+e^- \rightarrow q\bar{q}$	8
4.1	Decay diagram for the $\Upsilon(4S)$ state.	9
4.2	Invariant mass of the D^0 , obtained from the π^+ and the K^-	12
4.3	Purity determination of the D^0 invariant mass peak.	13
4.4	Correlation between the momenta of the D^0 and the slow pion π_s	16
4.5	Invariant mass of the D^{*+} , obtained from the D^0 and the slow pion.	17
4.6	Difference of the invariant masses of the D^{*+} and the D^0	17
4.7	Purity determination of the $M(D^{*+}) - M(D^0)$ mass difference peak.	18
4.8	z_0 position difference between the signal and tag lepton's origin.	19
4.9	z_0 position of the D^{*+}	20
4.10	Correlation between the origins of the signal lepton ℓ_s and the D^{*+}	20
4.11	Visible part of the mass of the signal B^0 meson.	21
4.12	Correlation between the origins of the signal lepton ℓ_s and the D^{*+} after applying all selection criteria.	22
5.1	Box diagrams of leading order $B^0\bar{B}^0$ transitions.	23
5.2	Asymmetry \mathcal{A} as a function of the time Δt between the two B decays.	25

List of Tables

4.1	Properties of the emerging mesons.	10
-----	--	----

Bibliography

- [1] Eckhard von Törne. *Particle-antiparticle oscillations at BELLE-II. Course Manual*. February 2022.
- [2] *Belle II Experiment*. URL: <https://www.belle2.de/en/belle-2-experiment> (visited on 24/04/2025).
- [3] S. Navas et al. (Particle Data Group). ‘Review of Particle Physics’. In: *Phys. Rev. D* 110.3 (2024), p. 030001. DOI: 10.1103/PhysRevD.110.030001.
- [4] Kavita Lalwani (Belle II). ‘The Belle II experiment: Status and prospects’. In: *SciPost Phys. Proc.* 8 (2023), p. 176. DOI: 10.21468/SciPostPhysProc.8.176.
- [5] Olivier Schneider. *B^0 - B^0 bar mixing*. 2000, last revision 2024. URL: <https://pdg.lbl.gov/2024/reviews/rpp2024-rev-b-bar-mixing.pdf>.